Supporting Information

Ambient pressure drying preparation strategy of biomimetic bagasse cellulose aerogel for atmospheric water harvesting

Fumeng Guo [a], Changhui Fu [a], Wentao Zhou [a], Jiawei Cui [a], Zhiguang Guo*[a, b]

a Ministry of Education Key Laboratory for the Green Preparation and Application of Functional Materials, Hubei University, Wuhan 430062, People's Republic of China.

b State Key Laboratory of Solid Lubrication, Lanzhou Institute of Chemical Physics, Chinese Academy of Sciences, Lanzhou 730000, People's Republic of China.

Corresponding Authors

Tel: 0086-931-4968105; Fax: 0086-931-8277088.

Email address: zguo@licp.cas.cn (Z Guo).

Note S1: Atmospheric Pressure Drying Theory

Atmospheric pressure drying is an efficient drying method that does not require extreme pressure or low temperatures, making it suitable for the large-scale production of aerogels. Its core principle involves regulating the force balance on pore walls during the drying process to prevent the collapse of porous structures, thereby achieving low-cost, low-energy consumption aerogel production.

This paper summarizes the theory, key strategies, and implementation pathways as follows[1]:

1. Theoretical Foundation: Stress Mechanism of Pore Walls During Drying During aerogel drying, solvent evaporation generates capillary pressure at the gas-liquid interface, which is transmitted through the pore walls and may cause pore structure collapse. The core mechanism is based on the Young-Laplace equation[2]:

$$P = \frac{-2\gamma\cos\theta}{r} \#(1)$$

where P is the capillary pressure, γ is the solvent surface tension, θ is the contact angle between the solvent and the pore wall, and r is the pore radius. During drying, the pore walls are subjected to unbalanced forces (such as N and N') generated by capillary pressure(Figure 2a). If the mechanical strength of the pore walls is insufficient or the surface tension of the solvent is too high, structural collapse may occur[3].

2. Key Strategies for Achieving Atmospheric Pressure Drying To balance pore wall stress and prevent structural collapse, the following two aspects must be regulated: Enhancing the mechanical properties of the pore network structure: Chemical cross-linking can be used to increase pore wall strength and resist capillary pressure compression. For example, chitosan (CS) can be used as a reinforcing agent, glutaraldehyde (GA) as a cross-linking agent, and sugarcane bagasse cellulose (BC) to form multiple chemical interactions, thereby strengthening the pore wall structure. The aldehyde groups (-CHO) in glutaraldehyde react with the hydroxyl groups (-OH) on the cellulose molecular chains to form hemiacetal or acetal structures, linking cellulose molecules via covalent bonds to enhance pore wall flexibility and deformation resistance. The aldehyde group (-CHO) of glutaraldehyde reacts with the amino group

(-NH_2) of chitosan via a Schiff base reaction to form carbon-nitrogen double bonds (C=N), creating rigid crosslinking points that further enhance the stability of the network structure. Hydroxyl groups (-OH) and amino groups (-NH_2) in chitin molecules form hydrogen bonds with cellulose molecules, working together with covalent bonds to create multiple forces that enhance the overall mechanical strength of the pore walls. Reducing the surface tension of the solvent: Replacing high-surface-tension solvents (such as water) through solvent exchange reduces capillary pressure. This study did not adopt traditional solvent exchange methods (such as replacing with low-surface-tension solvents) but instead employed a “freeze-curing - mild drying” process. By leveraging the physical form of ice crystals to weaken the negative impact of solvent surface tension on pore structure, combined with crosslinking-enhanced pore wall strength, the study achieved the stable retention of porous structure under atmospheric pressure drying.

3. Implementation Pathway for Atmospheric Pressure Drying Taking sugarcane bagasse cellulose aerogel as an example, the specific steps demonstrate the application of the aforementioned theory: the three-dimensional network structure formed by chemical cross-linking significantly enhances the mechanical properties of the pore walls, including collapse resistance. Cross-linked pore walls can withstand capillary pressure generated during atmospheric pressure drying due to solvent evaporation. Uncrosslinked structures are prone to pore collapse due to capillary forces during drying, whereas crosslinked BC/CS-CNT aerogels maintain their framework integrity during freeze-drying at atmospheric pressure (80°C), with hydrogen bonding forces further strengthened after ice crystal melting, ultimately forming a stable porous structure. Load-bearing capacity and flexibility: The crosslinked aerogel can withstand a load 1,000 times its own weight (500 g) without deformation and can be molded into various shapes, demonstrating the excellent mechanical stability and flexibility of its pore wall structure.

Note S2.Water adsorption kinetics theory

Water adsorption kinetics theory is a theoretical framework for studying the dynamic adsorption processes of water on and within material surfaces (including adsorption rates, mechanisms, equilibrium states, and influencing factors). Its core lies in revealing the time-dependent interaction patterns between water and materials. Specifically, this theory encompasses the following key elements[4]:

1. Adsorption mechanism. The water adsorption of LBC/CS-CNT materials stems from the synergistic effect of highly hygroscopic salts and a porous matrix: lithium chloride (LiCl) loaded in the aerogel serves as the core adsorbent component, undergoing deliquescence at a relative humidity of 11%, capturing water vapor from the air through strong interactions with water molecules to form crystalline hydrates such as $LiCl \cdot H_2O$; At the same time, the hydrophilic network framework formed by sugarcane bagasse cellulose and chitosan (such as the hydroxyl groups in sugarcane bagasse cellulose and the amino groups in chitosan), combined with the interaction with water molecules through hydrogen bonds, enhances the water uptake capacity. The three-dimensional interconnected microporous structure provides a diffusion channel for the adsorption of water molecules and forms a water storage space. The mechanical stability of the cross-linked network effectively prevents leakage of the lithium chloride solution. During the adsorption process, a significant osmotic pressure gradient exists between the material's surface and interior: the osmotic pressure decreases after surface adsorption, while the interior maintains a higher osmotic pressure. This concentration gradient serves as the driving force for continuous water diffusion into the material's interior, thereby accelerating the adsorption process.

2. Adsorption kinetics characteristics. The adsorption kinetics of water molecules comply with Fick's second law, with the adsorption rate primarily dependent on the diffusion speed within the aerogel. Fick's second law is one of the fundamental laws describing diffusion phenomena and has significant applications in the field of water adsorption kinetics. The mathematical expression for Fick's second law is:

$$\frac{\partial C}{\partial t} = D\left(\frac{\partial^2 C}{\partial x^2} + \frac{\partial^2 C}{\partial y^2} + \frac{\partial^2 C}{\partial z}\right) \#(2)$$

which can be simplified to in one-dimensional cases:

$$\frac{\partial C}{\partial t} = D\left(\frac{\partial^2 C}{\partial x^2}\right) \#(3)$$

C represents the concentration of the substance (e.g., water molecules), indicating the number or mass of water molecules per unit volume. t represents time, describing the duration of the adsorption process. D is the diffusion coefficient, which reflects the ability of water molecules to diffuse in the medium. It is related to the properties of the medium (such as pore structure, material type) and factors like temperature. The larger the pores in the medium and the better the connectivity, the larger the diffusion coefficient is typically. As temperature increases, molecular thermal motion intensifies, and the diffusion coefficient also increases. x (along with y and z in three-dimensional expressions) represents spatial coordinates, used to determine the spatial distribution of concentration. This law states that during diffusion, the rate of change of substance concentration at a point over time is proportional to the second spatial derivative of concentration, meaning that the change in concentration over time depends on the spatial distribution of concentration and the diffusion coefficient.

The calculation of Dab is based on a simplified model of Fick's second law, with the specific steps as follows:

Fick's second law is used to describe the diffusion behavior of the adsorbate in spherical adsorbents, and its linearized expression is:

$$\ln\left(1 - \frac{M_t}{M_e}\right) = \ln\left(\frac{6}{\pi^2}\right) - \frac{D_{ab} \cdot \pi^2}{d^2} \cdot t \#(4)$$

Where,Mt and Me represent the water content at time t and equilibrium state, respectively, and d is the thickness of the adsorbent.

Fitting slope calculation: The slope (k) of the straight line is obtained through linear fitting of the figure 4h and the relationship between the slope and the diffusion

coefficient is:

$$k = -\frac{D_{ab} \cdot \pi^2}{d^2} \#(5)$$

Reverse calculation of the diffusion coefficient based on the slope:

$$D_{ab} = \frac{|k| d^2}{\pi^2} \#(6)$$

Note S3. Water Desorption Kinetic Theory

The theory of water desorption kinetics primarily investigates the release rate, mechanisms, and influencing factors of adsorbed water in adsorbent materials, with the core objective of elucidating the process by which materials desorb water. The energy-driven mechanism of desorption requires overcoming intermolecular interactions between water molecules and the material (such as hydrogen bonds and ionic bonds), which necessitates external energy input[5].

1. The desorption process of LBC/CS-CNT relies on the photothermal conversion effect of carbon nanotubes (CNTs): CNTs can efficiently convert solar energy into thermal energy, thereby disrupting the bonding force between water molecules and the material, promoting water evaporation and desorption. Designing a hydrophilic network structure can reduce the desorption activation energy. The material structure directly influences the desorption kinetics, as its porous structure and network stability directly affect water transport efficiency, thereby determining the desorption rate. LBC/CS-CNT forms a three-dimensional porous network and interconnected micron-sized pores as mass transfer pathways through atmospheric pressure drying. The pore structure retained after ice crystal melting provides a rapid pathway for water migration, effectively reducing mass transfer resistance. The porous structure prevents lithium chloride agglomeration from blocking channels, ensuring efficient water diffusion from the interior to the surface. The Schiff base reaction between chitosan and glutaraldehyde (C=N bond) and hydrogen bonding between cellulose and chitosan enhance network structural stability, preventing pore collapse during drying or desorption and maintaining the continuity of mass transfer pathways. This enables the material to maintain efficient desorption performance even after loading with lithium chloride.

2. A quantitative desorption kinetic model based on Fick's second law. This model quantifies the water release rate using Fick's second law, with its core parameter, the diffusion coefficient Dad, characterizing the water diffusion capability within the material. The calculation of Dad is based on the diffusion behavior of the desorption process described by Fick's second law, with the specific calculation steps as follows:

Model selection: During desorption, the adsorbate diffuses from the interior of the

material to the surface. The short-time approximation solution (single-sided diffusion) of Fick's second law is:

$$\frac{(M_t - M_e)}{(M_0 - M_{e)}} = 1 - \frac{2}{d}\left(\frac{D_{ad}t}{\pi}\right)^{\frac{1}{2}} \#(7)$$

where Mt, Me, and M_0 represent the water content at time t, equilibrium state, and initial state, respectively, and d is the thickness of the adsorbent.

Fitting slope calculation: The slope (k) of the linear fit of the 5d plot is obtained, and the relationship between the slope and the desorption diffusion coefficient is:

$$k = -\frac{2}{\sqrt{\pi}} \cdot \frac{\sqrt{D_{ad}}}{d} \#(8)$$

Deriving the desorption diffusion coefficient from the slope:

$$D_{ad} = \frac{k^2 \cdot d^2 \cdot \pi}{4} \#(9)$$

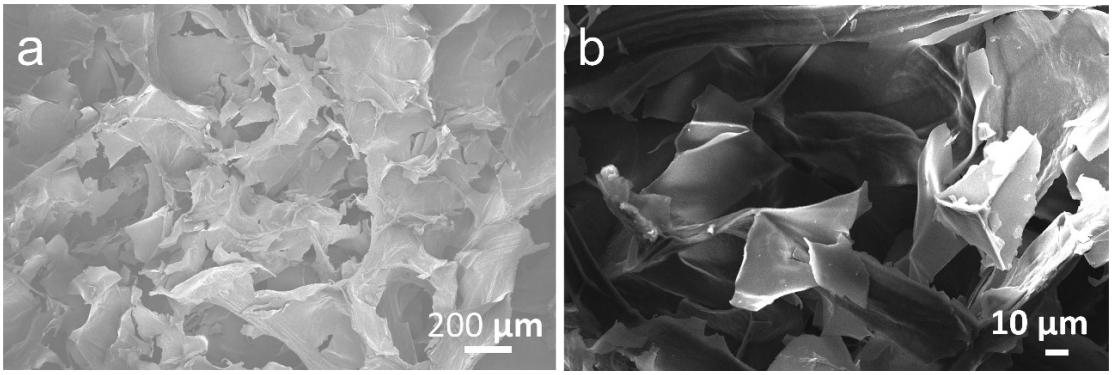

Figure S1. (a-b) SEM images and further magnified SEM images of BC/CS aerogel with smooth surface.

Figure S2. Deformation of aerogel under different weights.

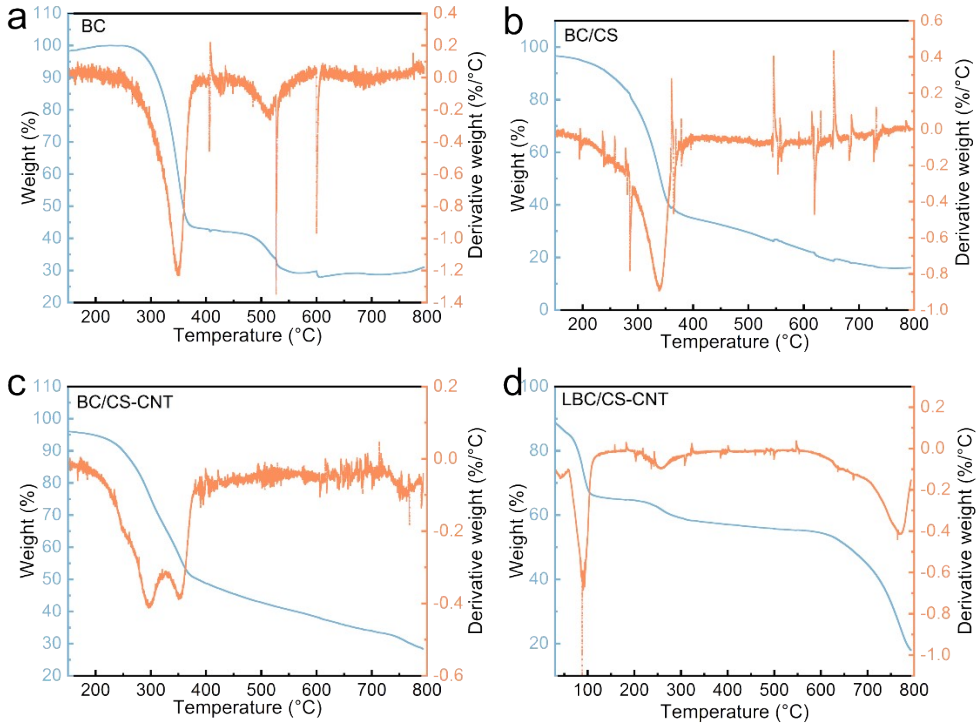

Figure S3. (a) TGA results for BC and corresponding DTG curves. (b) TGA results for BC/CS and corresponding DTG curves. (c) TGA results for BC/CS-CNT aerogel and corresponding DTG curves. (d) TGA results for LBC/CS-CNT aerogel and corresponding DTG curves.

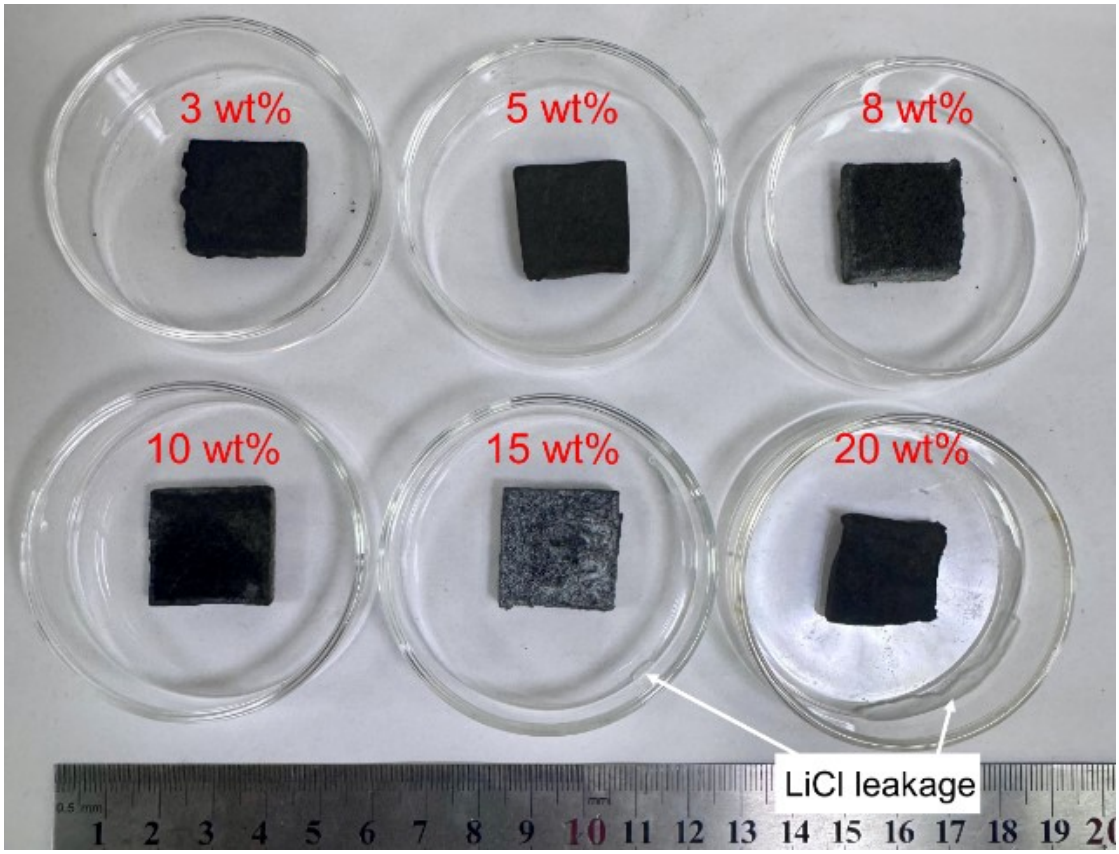

Figure S4. Optical photographs of LBC/CS-CNT aerogels soaked in lithium chloride solutions with concentrations of 3 wt%, 5 wt%, 8 wt%, 10 wt%, 15 wt%, and 20 wt% after drying for 12 hours at 90% RH and 25°C.

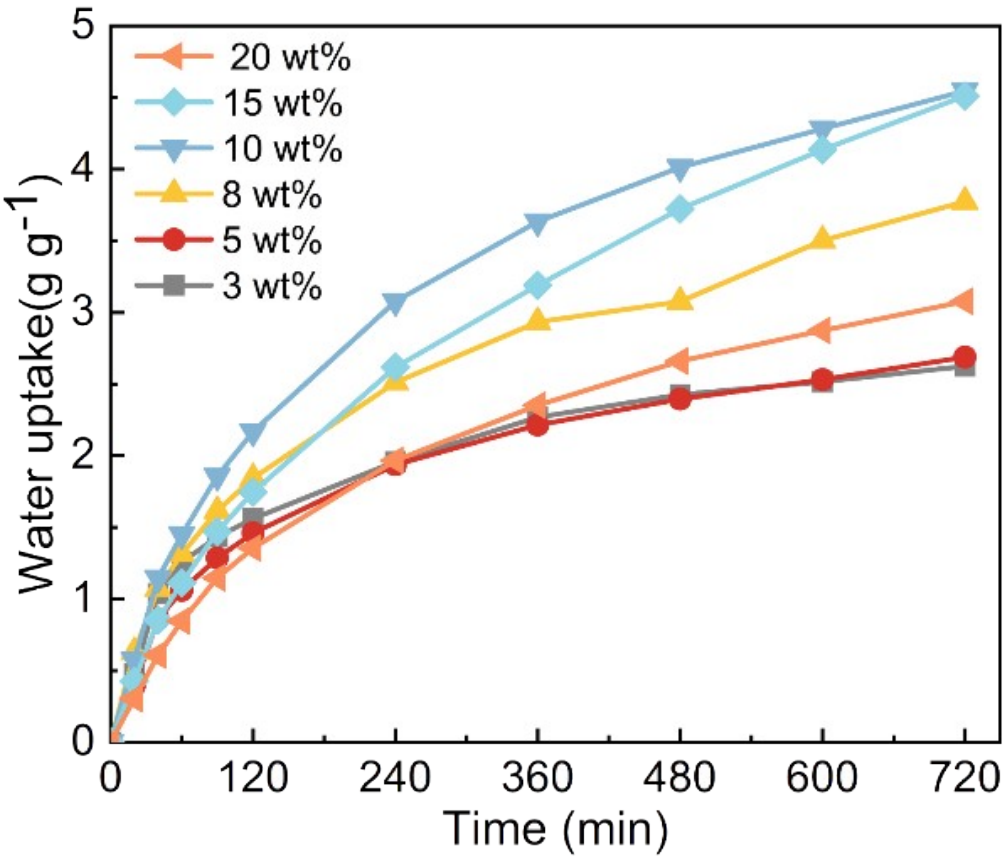

Figure S5. Comparison of moisture absorption of LBC/CS-CNT aerogel after 12 hours of moisture absorption at 90% RH and 25°C in lithium chloride solutions with immersion concentrations of 3 wt%, 5 wt%, 8 wt%, 10 wt%, 15 wt%, and 20 wt%.

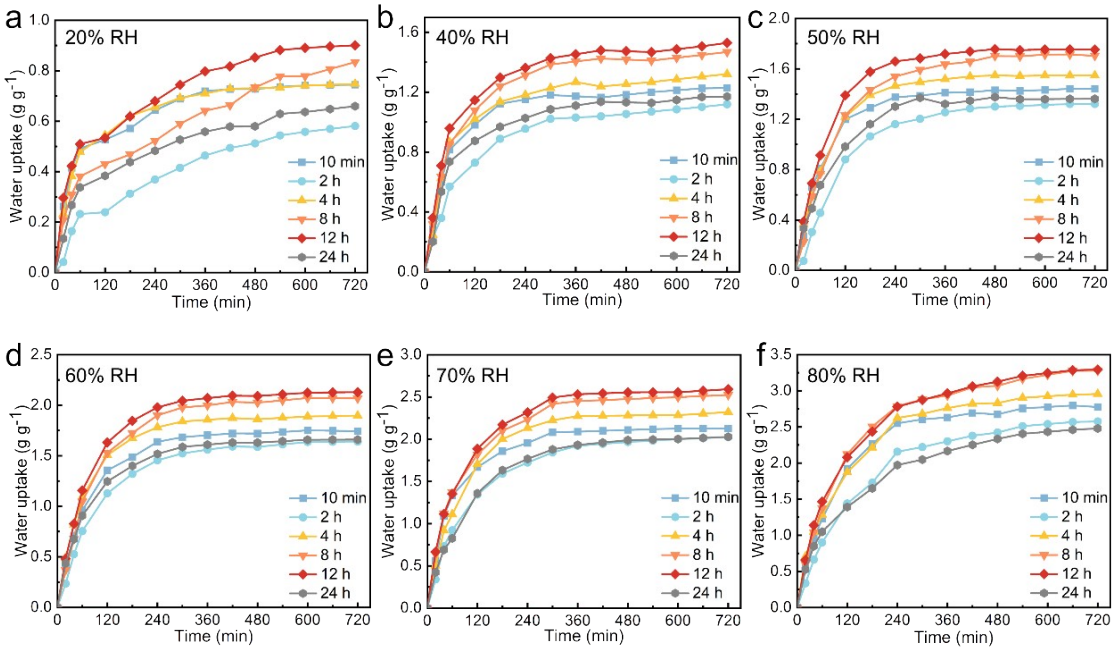

Figure S6. Water uptake of LBC/CS-CNT aerogel samples immersed in 10 wt% lithium chloride solution for different durations under conditions of 20–90% RH and 25°C after 12 hours of moisture absorption.

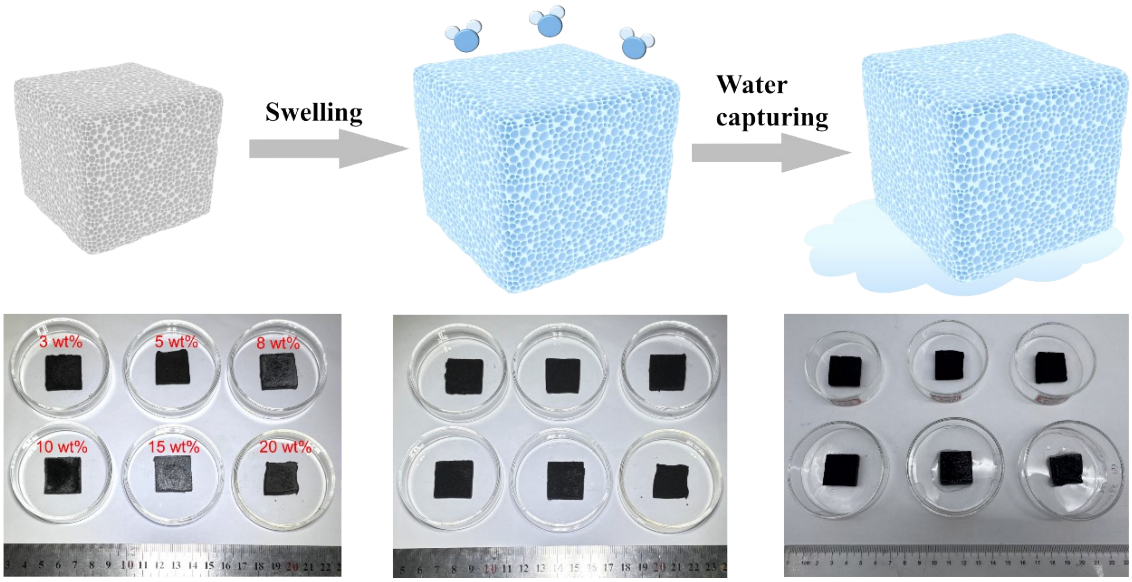

Figure S7. Optical photographs of LBC/CS-CNT aerogel after 4 hours and 12 hours of water absorption under conditions of 90% RH and 25°C.

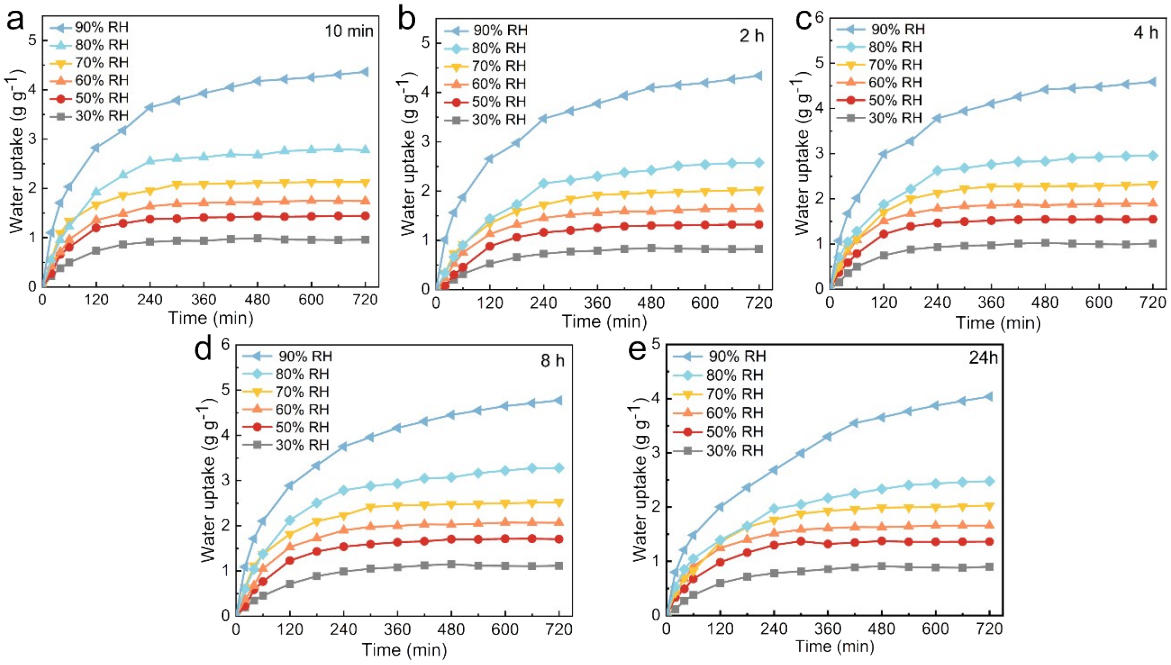

Figure S8. Water uptake of LBC/CS-CNT aerogel after soaking in 10 wt% lithium chloride solution for 12 hours, followed by 12 hours of water absorption at 20–90% RH and 25°C.

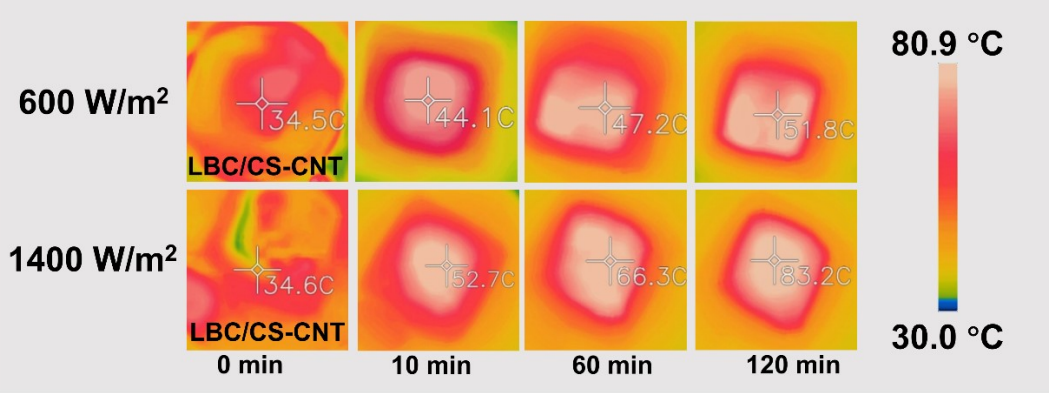

Figure S9. Infrared thermal imaging of the LBC/CS-CNT aerogel surface after moisture absorption under light intensities of 600 W/m² and 1400 W/m², and the final temperature field within 2 hours of irradiation.

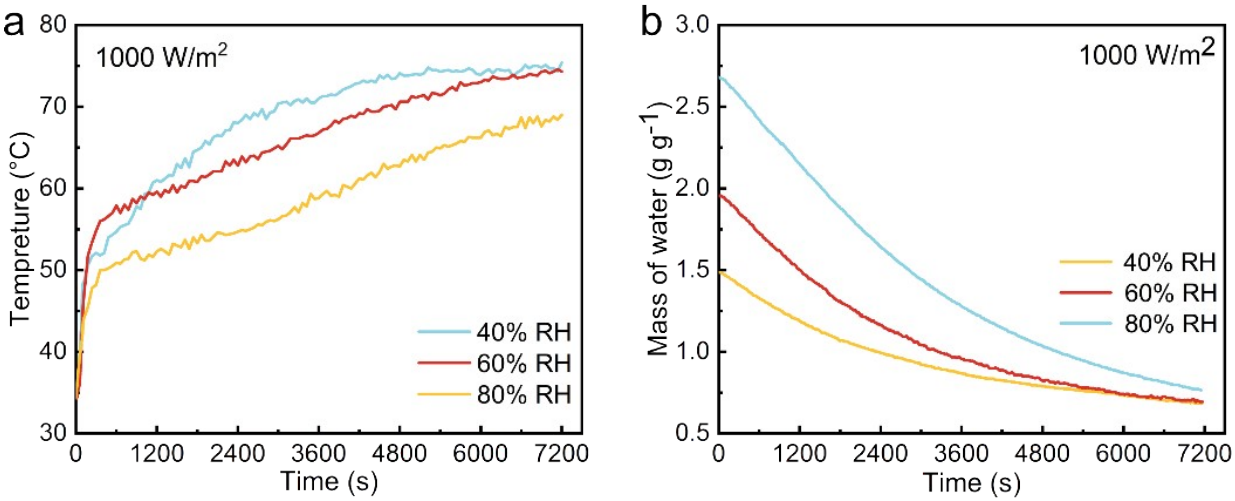

Figure S10. (a) Temperature changes in LBC/CS-CNT aerogel after 2 hours of irradiation at 1000 W/m² light intensity following moisture absorption saturation at 40% RH, 60% RH, and 80% RH, 25°C. (b) Change in evaporation mass of LBC/CS-CNT aerogel after 2 hours of exposure to 1000 W/m² light intensity following moisture absorption saturation at 40% RH, 60% RH, and 80% RH at 25°C.

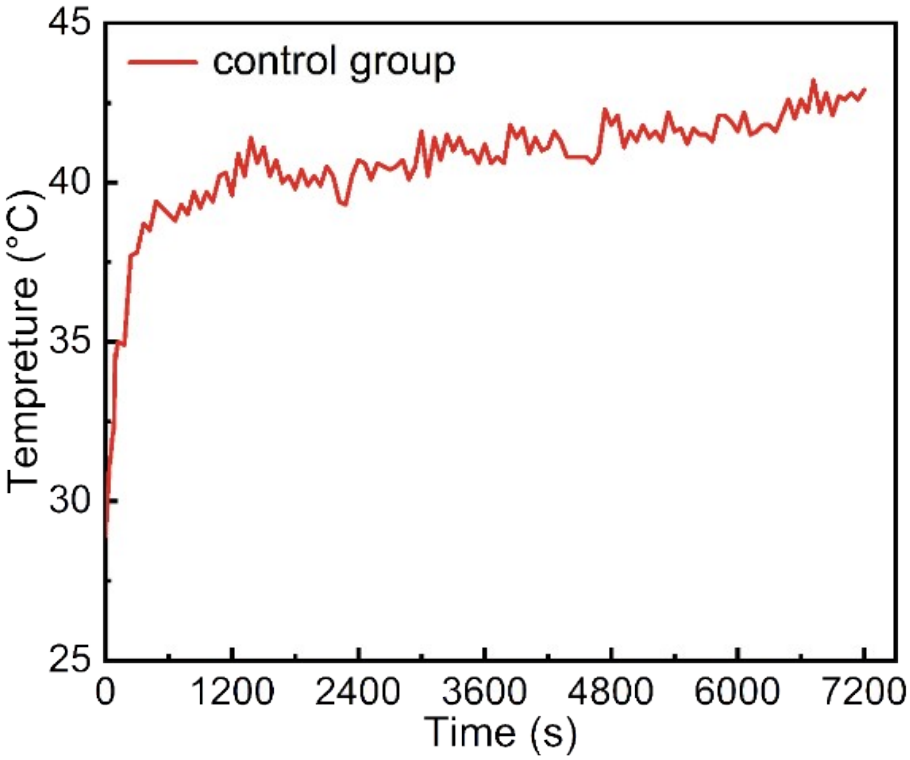

Figure 11. Infrared thermal imaging of the LBC/CS aerogel surface after moisture absorption under an illumination intensity of 1000 W/m^2 and the final temperature field within 2 hours of irradiation.

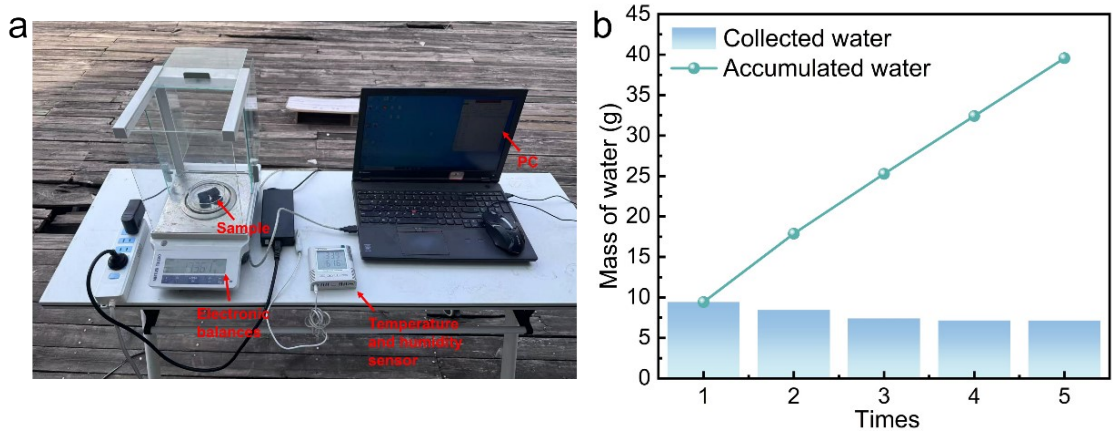

Figure S12. a) Schematic diagram of the nighttime water vapor adsorption device. b) Five solar desorption processes conducted during the day on LBC/CS-CNT samples.

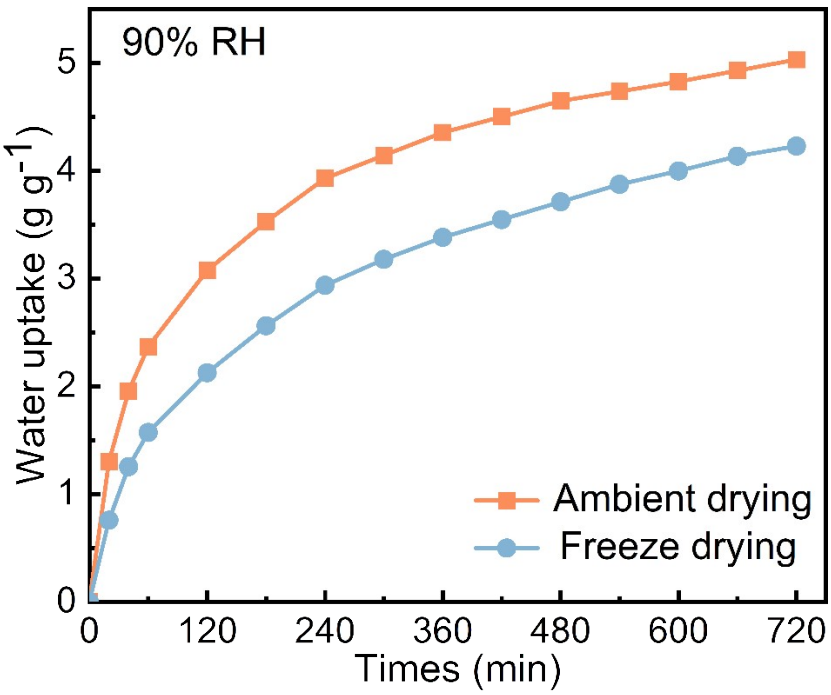

Figure S13. Water uptake curves of ambient-pressure dried aerogels and freeze-dried aerogels at 25 ℃ and 90% RH.

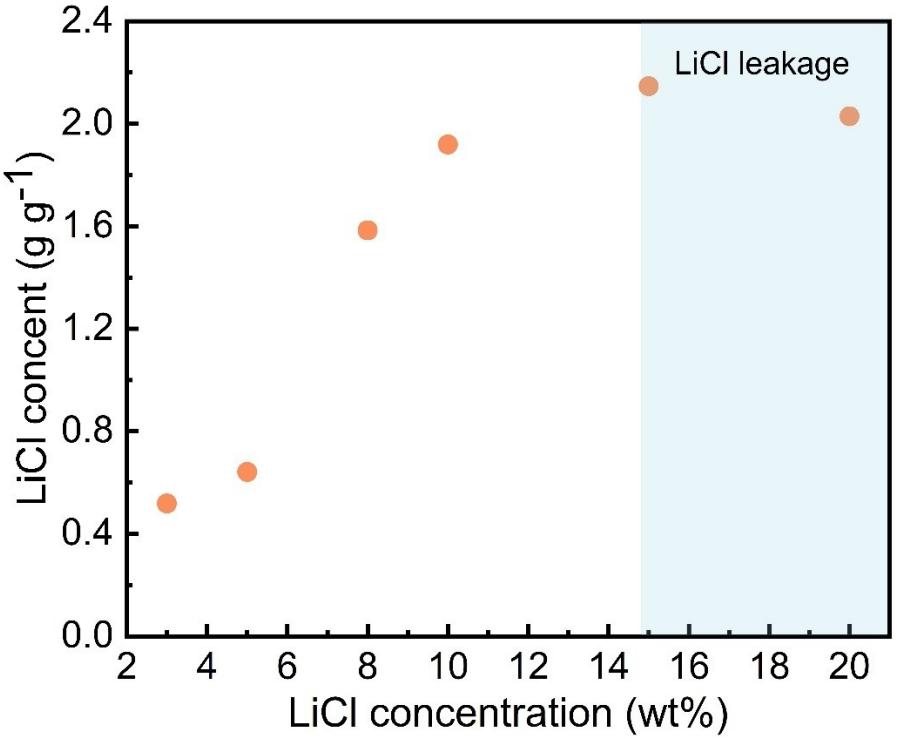

Figure S14. The LiCl content in aerogels immersed in LiCl solutions of varying concentrations.

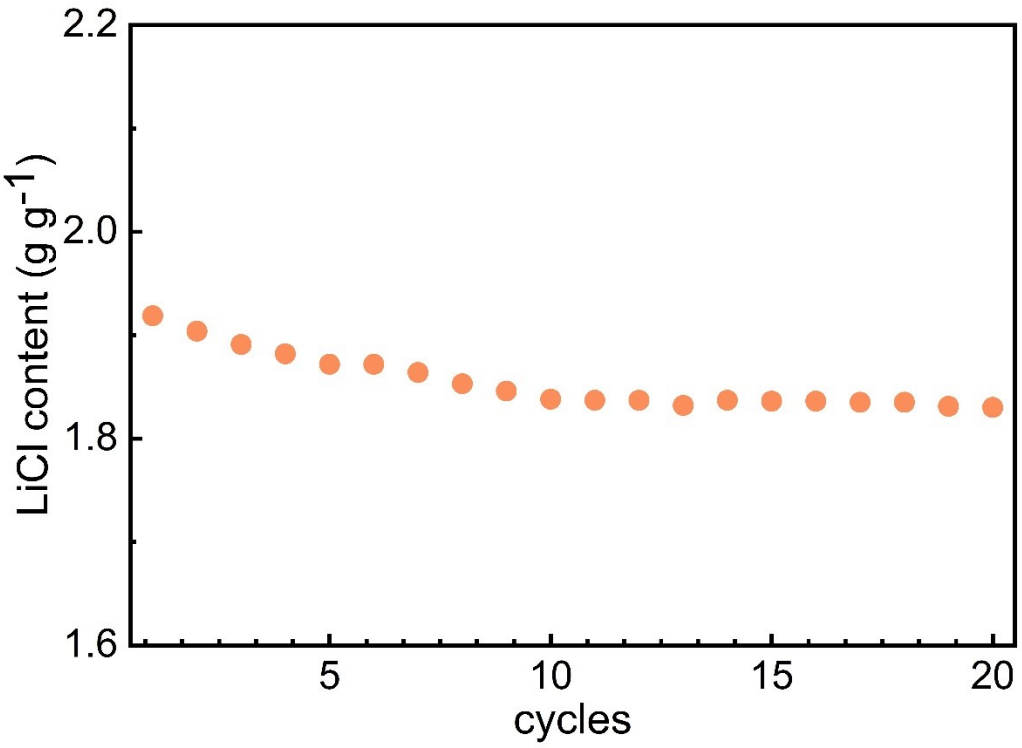

Figure S15. LiCl content in aerogel after 20 cycles of testing.

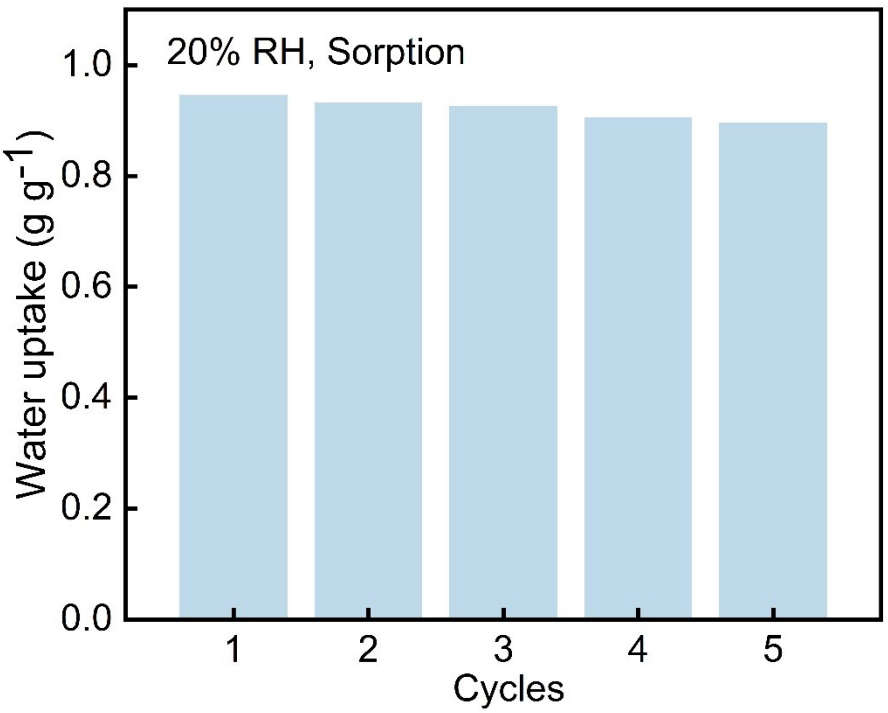

Figure S16. Performance of aerogel undergoing 5 adsorption/desorption cycles at 20% RH.

Table S1. Comparison of moisture absorption properties of materials reported in other literature for use in AWH.

AWH materials	RH (%)	Water uptake (g/g)	References
CNF/LiCl-scaffold	33	0.6	[6]
	57	12	
	75	1.5	
CNF/SA@MAc-P	35	0.58	[7]
	50	0.99	
	70	1.20	
	90	2.18	
Core-Shell@CNF	30	0.48	[8]
	60	0.68	
	90	1.16	
LHST	20	0.70	[9]
	30	0.94	
	40	1.10	
NHDM-50	30	0.57	[10]
	50	0.70	
	65	1.11	
CGH	20	0.78	[11]
	40	1.05	
	60	1.38	
PAMS-CNT-LiCl	30	1.00	[12]
	60	1.87	
SMPH	30	0.49	[13]
	50	0.91	
	70	1.45	
	90	2.98	
	20	0.63	

AWH materials	RH (%)	Water uptake (g/g)	References
CAL gel	30	0.79	[14]
	30	0.68	
	60	1.61	
	70	1.92	
PPA@PP-Cl	80	2.47	[15]
	90	2.76	
	20	0.75	
	40	0.83	
	60	1.1	
LCSC-MC	80	2	[16]
	90	3.85	
	20	0.90	
	30	1.18	
	40	1.53	
LBC/CS-CNT	50	1.75	This work
	60	2.13	
	70	2.59	
	80	3.29	
	90	5.03	

References

1. N. Wu, Y. Yang, C. Wang, Q. Wu, F. Pan, R. Zhang, J. Liu and Z. Zeng, *Advanced Materials*, 2023, **35**, 2207969.
2. Y. Li, N. Grishkewich, L. Liu, C. Wang, K. C. Tam, S. Liu, Z. Mao and X. Sui, *Chemical Engineering Journal*, 2019, **366**, 531-538.
3. Y. Mao, Y. Sheng, Z. Fan, J. Yang, J. Liu, C. Tang and S. Fu, *Advanced Functional Materials*, 2025, **35**, 2421492.
4. J. Lu, J. Yan, F. Pei, Z. Niu, J. Li, G. Han, D. Wang, Y. Yue and W. Cheng, *Advanced Functional Materials*, **n/a**, 2505359.
5. J. Sun, F. Ni, J. Gu, M. Si, D. Liu, C. Zhang, X. Shui, P. Xiao and T. Chen, *Advanced Materials*, 2024, **36**, 2314175.
6. P. Zhu, Z. Yu, H. Sun, D. Zheng, Y. Zheng, Y. Qian, Y. Wei, J. Lee, S. Srebnik, W. Chen, G. Chen and F. Jiang, *Advanced Materials*, 2024, **36**, 2306653.
7. J. Wang, Z. Wei, C. Ren, B. Cai, Z. Wang, C. Cai and H. Lei, *Chemical Engineering Journal*, 2025, **512**, 162724.
8. Z. Yu, S. Li, J. Su, J. Zhang, D. Zhang, Z. Zhou, Z. Qin, X. Liu, Y. Lai and S. Fu, *Matter*, 2023, **6**, 3509-3525.
9. R. Zhu, Q. Yu, M. Li, A. Li, D. Zhan, Y. Li, Z. Mo, S. Sun and Y. Zhang, *Nano Energy*, 2024, **124**, 109471.
10. Y. Lee, S. H. Nah, K.-Y. Wang, Y. Chi, J. B. Kim, Z. Zhang and S. Yang, *Advanced Functional Materials*, **n/a**, 2506725.
11. Q. Luo, T. Zhang, M. Chen, C. Gao, L. Guo, M. Zhou, L. Zhu, H. Wei, A. Khan, Y. Hou and Y. Zheng, *Small*, 2025, **21**, 2503948.
12. H. Shan, P. Poredoš, Z. Ye, H. Qu, Y. Zhang, M. Zhou, R. Wang and S. C. Tan, *Advanced Materials*, 2023, **35**, 2302038.
13. X. Wang, G. Ma, S. Cui, K. Sun, W. Li and H. Peng, *Small*, 2024, **20**, 2307416.
14. H. Zhou, L. Yan, D. Tang, T. Xu, L. Dai, C. Li, W. Chen and C. Si, *Advanced Materials*, 2024, **36**, 2403876.
15. Z. Zhang, Y. Wang, Z. Li, H. Fu, J. Huang, Z. Xu, Y. Lai, X. Qian and S. Zhang, *ACS Applied Materials & Interfaces*, 2022, **14**, 55295-55306.
16. C. Fu, Y. He, A. Yu, G. Tian, D. Zhan, H. Zhang and Z. Guo, *Journal of Materials Chemistry A*, 2024, **12**, 33926-33938.